nature materials

SUPPLEMENTARY INFORMATION

DOI: 10.1038/NMAT4429

# Reversible dilatancy in entangled single-wire materials

David Rodney[1,2], Benjamin Gadot[2,3], Oriol Riu Martinez[3], Sabine Rolland du Roscoat[3] & Laurent Orgéas[3]

[1] Institut Lumière Matière, Université Lyon 1-CNRS, F-69622 Villeurbanne, France
[2] SIMAP, Université Grenoble Alpes-CNRS, F-38000 Grenoble, France
[3] 3SR Lab, Université Grenoble Alpes-CNRS, F-38000 Grenoble, France

DOI: 10.1038/NMAT4429

## I- Experimental processing route

The experimental processing route is adapted from the work of Tan et al (Ref. 32 of the main text) and detailed in the case of NiTi wires in Ref. 35 of the main text. We show below an example of the processing steps for a polyamide wire. A small section of the wire (500 μm in diameter) is shown in Supplementary Figure 1(a) (the full wire is about 20 m long). The wire is then rolled around a 3 mm threaded bar with a pitch close to the wire diameter (Supplementary Figure 1(b)) and fixed at its extremities using bolts. This assembly is then heated at 160°C during 15 min to set the coiled shape of the wire. Once the extremities are released, a small elastic spring-back of the wire slightly separates the wire from the threaded bar, which allows to easily remove the coil (Supplementary Figure 1(c)). The coiled wire is then loosely entangled around a 3 mm rod (Supplementary Figure 1(d)), to obtain a loose fibrous ball, which can be easily removed from the rod (Supplementary Figure 1(e)). During this operation, a large degree of entanglement was ensured with disordered fiber segment placement and orientation by (i) subjecting the coiled wire to a slight extension in order to open its dense helical structure and to allow it to efficiently entwine with the segments already present in the ball (ii) by randomly varying the winding angle of the centerline of the coiled wire with respect to that of the rod. In order to set the final shape of the sample and remove memory of for instance the rod axis used to formed the ball, the loose ball is compressed in a compression die at 160°C during 60 min (Supplementary Figure 1(f)). We checked in Ref. 35 that the relative density inside the sample is homogeneous and in Section III of the SI below, that the wire segment and contact orientation matrices are isotropic in the initial samples before deformation.

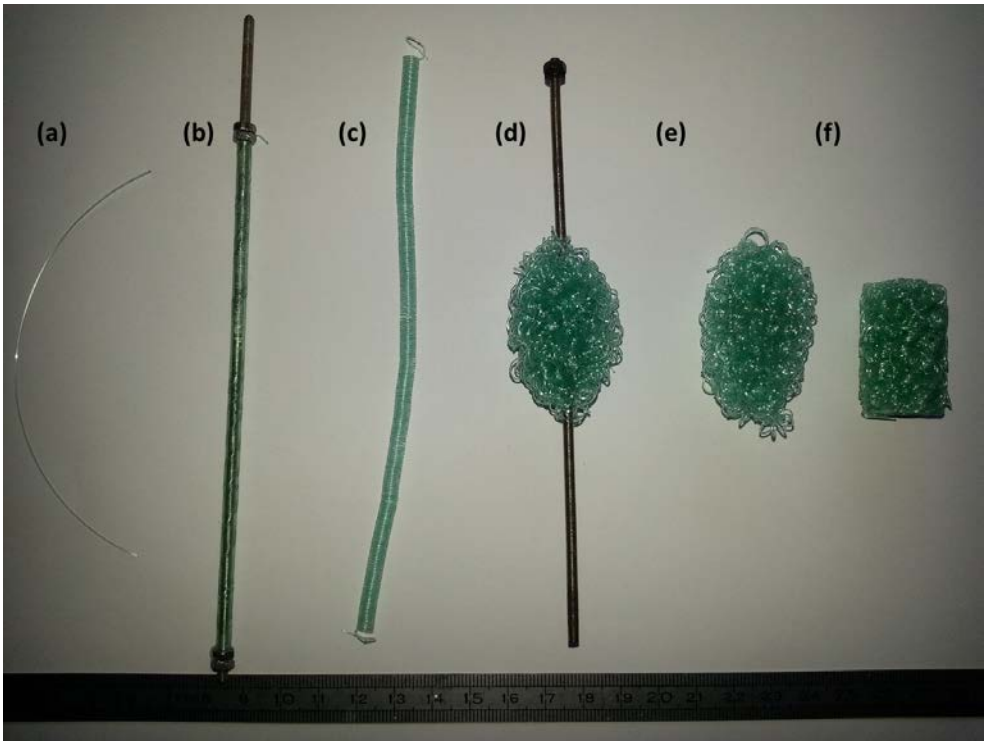


**Supplementary Figure 1. Processing route for the entangled single-wire materials.** Illustration on a polyamide wire (see text for details).

## II- Compressive dilatancy in glasses

In order to highlight the difference in compressive dilatancy between a single-wire system and a glass, we simulated the quasistatic uniaxial tension and compression of a glass model, composed of a binary mixture of atoms interacting with Wahnström parametrization of the Lennard-Jones potential [1,2]. The glass is made of 10,000 particles in a cubic periodic simulation cell, quenched from the liquid at a rate of $6\ 10^{-5}$ LJ units. Volumetric strains are shown in Supplementary Fig. 1. The deformation is composed of elastic segments where the volume decreases in compression and increases in tension, separated by plastic events that relax part of the internal stress by increasing the volume in compression and decreasing the volume in tension.

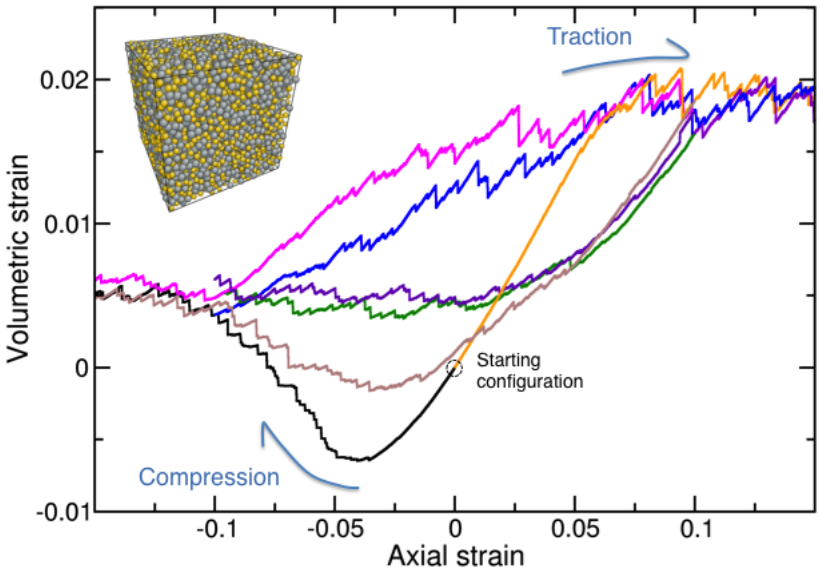


**Supplementary Figure 1. Compressive dilatancy in a model glass.** Variation of the volumetric strain during successive cycles of compressions and tensions of a glass model shown in the inset. The starting configuration at zero applied strain is indicated in a dashed circle. Arrows show the sense of the cycles.

During the first compression (black curve), the volume initially decreases in the elastic regime, then increases when the glass enters the plastic regime before reaching a plateau at large strains. This is the well-known process of dilatancy. Upon decompression (blue curve), dilatancy is irreversible and the volume continues to increase until it reaches an upper plateau. A recompression (green curve) and subsequent reloading (magenta and violet curves) induce only a decrease of volume in compression and an increase of volume in tension. The reason is that the first compression cycle has induced an irreversible evolution of the glass structure (often referred to as rejuvenation) that has brought the glass into a higher-energy, lower-density state where dilatancy is saturated. Upon reloading, no further dilatancy is produced and the volume simply varies between the 2 plateau values.

DOI: 10.1038/NMAT4429

## III- Evolution of anisotropy upon deformation

We consider here the evolution of the orientation distributions of the fiber segments and of the contacts between segments during deformation. Experimentally, we performed a compression test inside an X-ray microtomograph (3SR Lab/RX Solutions, Grenoble, France) on a NiTi sample with an initial relative relative density of 30%, in order to assess the evolution of the fiber and contact orientations. To get 3D in situ observations of the entangled mesostructure, seven scans at various compression strains were acquired during a load-unload compression sequence. After reconstruction followed by filtering and thresholding operations, we obtained 3D binarized images of the samples. The centerline of the wire was detected (i) using the 3D Euclidian distance map of the fibrous phase, (ii) thresholding the resulting grey scale image at an intermediate value to eliminate contact zones from the image, (iii) skeletonizing the thinned wire and (iv) smoothing the resulting skeleton to obtain its centerline (for more details, see Ref. 35 of the main text and references therein). The skeleton was then discretized in elementary segments of length, *2D*, i.e. twice the wire diameter. For each segment, $i = 1,N$, we computed the unit tangent vector, $\vec{n}(i)$, from which we deduced the second order fiber orientation tensor, $\overline{\overline{A}}$, such that:

$$A_{I,J} = \left\langle n_I(i) n_J(i) \right\rangle_{i=1,N} \text{ where } I, J=1, 2, 3.$$

Supplementary Fig. 5 shows the evolution of the component $A_{3,3}$ along the compression axis and $A_{1,1}$ in the lateral direction (the non diagonal components of $\overline{\overline{A}}$ are not plotted since they are close to 0; also, by construction, $A_{2,2} = 1 - A_{1,1} - A_{3,3}$). The same analysis was also performed on the numerical cylindrical sample during quasistatic deformation. The corresponding evolution of the orientation tensor is also shown in Supplementary Fig. 5 showing a very good agreement between the simulations and the experiments.

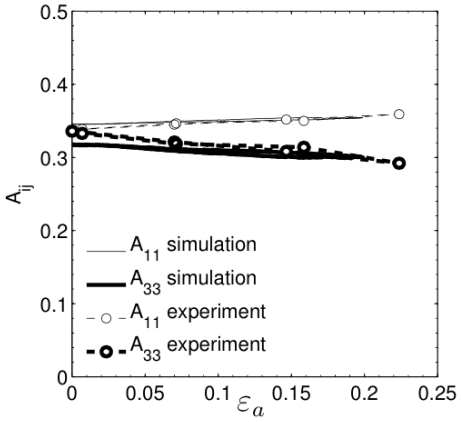


**Supplementary Figure 2. Evolution of segment orientation during deformation.** The components along the compression axis $A_{3,3}$ and in the lateral direction $A_{1,1}$ are shown as a function of the compressive strain. The experimental data were obtained after skeletonization of a reconstructed tomographic image of a NiTi sample. The numerical data were obtained on the compression of a cylindrical sample with initial mesostructure parameters close to the experimental sample.

We see that in the initial configuration at zero strain, all components are close to 1/3, confirming the isotropy of the initial configuration (see also Ref. 35 of the main text for more details on the full orientation tensor). Under compression, the axial component, $A_{3,3}$, decreases while the lateral component, $A_{1,1}$, increases, meaning that, as expected, the fiber segments rotate away from the compression axis and tend to flatten horizontally. We also note the very good agreement between simulations and experiments.

Self-contacts were defined as pairs of elementary segments with a distance less than the fiber diameter. Each contact, $j = 1,M$, was then ascribed an orientation unit vector $\vec{t}(j)$, normal to the contact plane, from which we deduced the second order contact orientation tensor $\overline{\overline{B}}$:

$$B_{I,J} = \left\langle t_I(j) t_J(j) \right\rangle_{j=1,M}$$

Supplementary Fig. 6 shows the evolution of the components of this tensor parallel and perpendicular to the compression axis both in the experimental and numerical samples (the non diagonal components of $\overline{\overline{B}}$ are not plotted because they are close to 0 and $B_{2,2}$ =1-$B_{1,1}$-$B_{3,3}$ by construction). We see that the lateral component, $B_{1,1}$, decreases, while the axial component, $B_{3,3}$, increases, meaning that in compression, the contacts rotate towards the deformation axis, i.e. the contacts created during the deformation are mostly oriented vertically and therefore directly participate in the mechanical response of the samples.

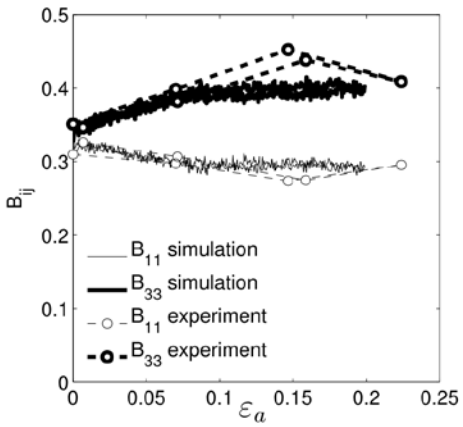


**Supplementary Figure 3. Evolution of contact orientation during deformation**. Same graphs as in previous Figure, but showing the orientation tensor components, $B_{1,1}$ and $B_{3,3}$.

DOI: 10.1038/NMAT4429

The same type of analysis was carried out on the reference periodic configuration, both in compression and tension. Supplementary Fig. 7 shows the evolution of the segment orientation tensor, where we recover that the axial component decreases in compression and increases in tension, meaning that, as expected, the segments rotate away from the deformation axis in compression and towards the deformation axis in tension. However, the increase in tension is much slower than the decrease in compression, implying that the segment rotation is slower in tension than in compression. The reason is the different natures of the contacts formed in compression and tension (see the discussion in the main text). The lateral components remain close, meaning that the sample remains transversely isotropic. The slight differences are due to the finite size of the sample.

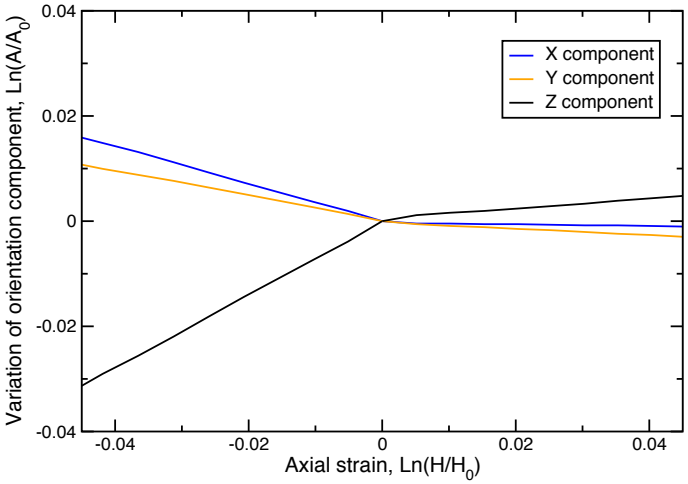


**Supplementary Figure 4. Evolution of segment orientation during deformation**. The diagonal components of the texture matrix of the fiber segments are shown during the compression and tension of the reference periodic configuration.

For the contact orientation tensor, we note that the above definition does not differentiate between weak contacts that come in large numbers in the simulations because the repulsive contact potential vanishes at the fiber diameter and strong contacts that play a real role in the mechanical response of the structure. For this reason, we prefer to weight these measures by the norm of the contact force, which is proportional to $\left(1-r_i/d\right)^{1.5}$ given the Hertzian form of the contact potential (see ref. 38 of the main text). In Supplementary Fig. 8, we plot the weighted number of contacts, $\sum_i \left(1-r_i/d\right)^{1.5}$, and the weighted texture matrix components

$$B'_{I,I} = \frac{\sum_i t_I(i) t_I(i) \left(1 - \frac{r_i}{d}\right)^{1.5}}{\sum_i \left(1 - \frac{r_i}{d}\right)^{1.5}}.$$

We see in Supplementary Fig. 8(a) that the number of contacts increases both in compression and tension but more rapidly in compression than in tension. Also, Supplementary Fig. 8(b) shows that there is a clear asymmetry in compression between the axial direction, Z, and the lateral directions X and Y. Indeed, the axial texture matrix component, $B'_{Z,Z}$, increases in compression while the lateral components slightly decrease. By way of contrast, in tension, all texture components remain close, implying that the contact distribution remains isotropic. These plots show that compression produces a large number of contacts that tend to orient vertically to resist the applied strain, while in tension, the contact number increases slowly in number and the contacts remain isotropic (with a scatter related to the small size of the sample), implying that they play a limited role in the mechanical response of the structure (see also the discussion in the main text).

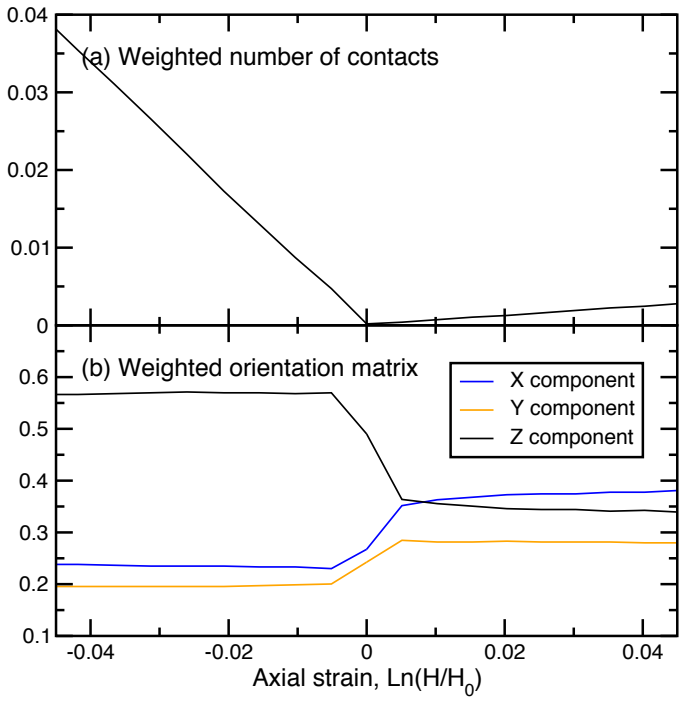


**Supplementary Figure 5. Evolution of contact orientation during deformation.** (a) Evolution of the weighted number of contacts, $\sum_i (1 - r_i/d)^{1.5}$, where the sum runs over all contacts detected in the structure, $r_i$ is the contact length and $d$ is the fiber diameter. (b) Diagonal elements of the weighted contact texture matrix, $B'_{I,I} = \left(\sum_i t_I(i)^2 (1 - r_i/d)^{1.5}\right) \Big/ \left(\sum_i (1 - r_i/d)^{1.5}\right)$ with *I=X, Y, Z*. The data were obtained during the tension and compression of the reference periodic configuration.

DOI: 10.1038/NMAT4429

## IV- Construction of the initial numerical samples

We describe here how the numerical samples were initially produced. Two different procedures were used for the cylindrical and periodic samples.

As illustrated in Supplementary Figure 2, the cylindrical samples were constructed in 3 steps, which qualitatively mimic the experimental procedure. To impose a cylindrical shape, we add an external repulsive potential $V_{cyl}$, which acts on the nodes when they reach the cylinder surface. Mathematically, the potential is expressed as:

$$V_{cyl}(r,z) = A \cdot H\left(z - H/2 + d\right)\left(1 - \frac{z - H/2 + d}{d}\right)^{\frac{5}{2}} +$$
$$A \cdot H\left(-H/2 + d - z\right)\left(1 - \frac{-H/2 + d - z}{d}\right)^{\frac{5}{2}} +$$
$$A \cdot H\left(r - R + d\right)\left(1 - \frac{r - R + d}{d}\right)^{\frac{5}{2}}$$

where $r = \sqrt{x^2 + y^2}$ . A is a numerical parameter, which fixes the strength of the repulsive potential, set to $A = 8Ed^4$ , with $E$, Young's modulus and $d$, the fiber diameter.

As illustrated in Supplementary Figure 2(a), initially, we start by constructing a random tube inside a cylinder of large dimensions ($R_0$=25mm, $H_0$=50mm). The tube has a diameter equal to the diameter of the final helix. The tube is relaxed by energy minimization in presence of the cylinder potential, but in absence of twist contribution and contacts between tube elements. This step is simply to obtain a first fiber structure of reasonnable curvature contained inside the cylinder. As illustrated in Supplementary Figure 2(b), we then construct a helix inside the tube by constructing inside each tube element an elementary helix connected to the helix elements in the neighboring tube segments. The configuration is then relaxed again at constant volume accounting for bending, twist and contacts, to obtain a loose mesh as in the experiments. The final step shown in Supplementary Figure 2(c) is a quasistatic compression of the entanglement by reducing incrementally the dimensions of the outer cylinder down to the final size (R=10mm, H=20mm). The cylindrical repulsive potential ensures that the entanglement remains inside the cylinder. The final configuration is then set as an equilibrium configuration by setting its current segment lengths and curvatures as equilibrium values and resetting the twist to zero. The cylindrical potential is then removed to obtain a free-standing equilibrium configuration that can be used as initial configuration for uniaxial tension and compression tests.

To impose the deformation, we control the altitude in the z-direction of the nodes that are within two fiber diameters from the top and bottom surfaces of the samples (nodes above and below the dashed lines in Supplementary Figure 2(c)). Their displacements in the x- and y-directions remain free in order to allow the sample to freely expand or contract laterally.

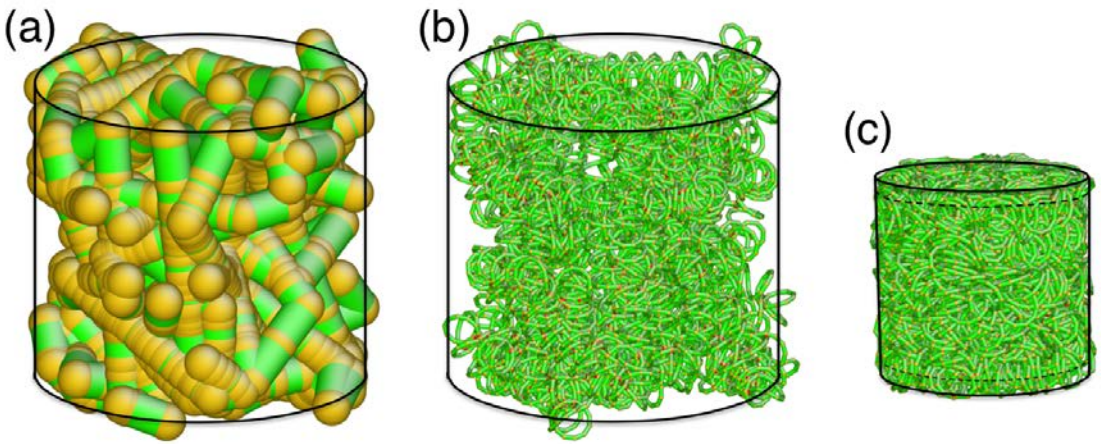


**Supplementary Figure 6. Construction of a numerical cylindrical sample.** (a) Initially, we construct a random tube inside a cylinder of large dimensions, modelled by a repulsive potential acting on the nodes that reach the cylinder surface. The tube is relaxed by energy minimization not accounting for contacts. (b) A helix is constructed inside the tube and relaxed at constant volume to obtain a loose mesh as in the experiments. (c) The entanglement is compressed quasistatially down to the final size (R=10mm, H=20mm). The configuration in (c) is set as an equilibrium configuration and the cylinder is removed. Uniaxial tensions and compressions are modelled by controlling the altitude of the nodes near the top and bottom surfaces of the sample.

DOI: 10.1038/NMAT4429

To construct periodic samples, we used a different procedure. As illustrated in Supplementary Fig. 3(a), we initially create the helix with the targeted length and radius as a large torus, with a radius, $R_{tore}$, much larger than the simulation cell size. We then apply the periodic boundary conditions inside the simulation cell, which forces the helix to fold onto itself, therefore creating numerous contacts, as illustrated in Supplementary Fig. 3(b). This configuration is then relaxed at fixed volume accounting for bending, twist and contacts. The configuration thus obtained is set as an equilibrium configuration by setting its current segment lengths and curvatures as equilibrium values and resetting the twist to zero. Note however that neither the curvature nor the segment lengths vary significantly during the relaxation. The configuration thus contains a single coiled fiber, which comes in and out of the simulation cell through the periodic boundary conditions and interacts with itself at the contact points.

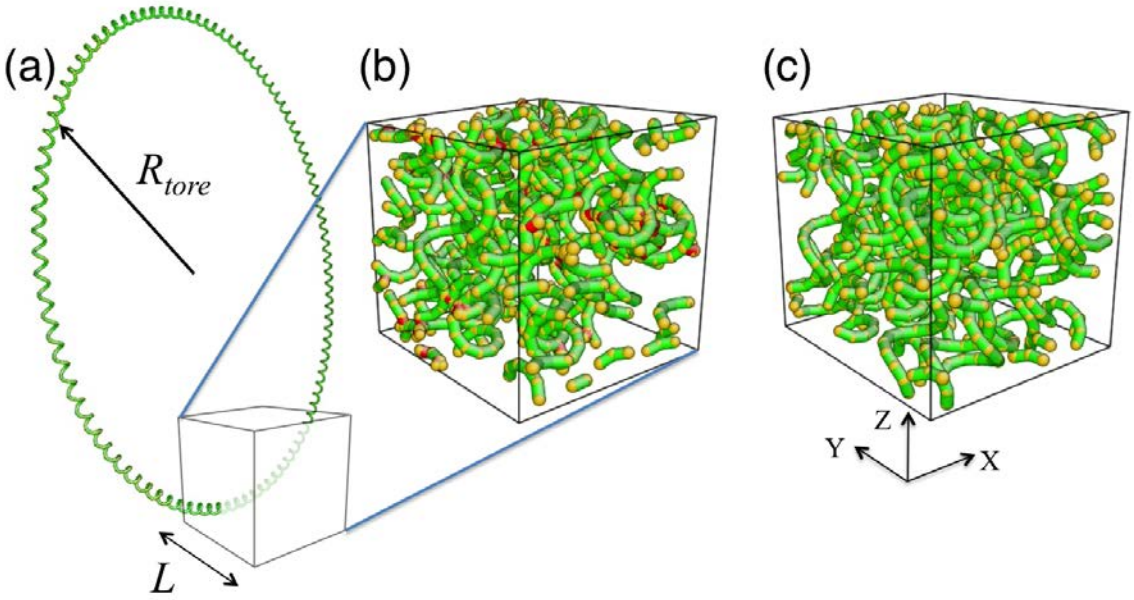


**Supplementary Figure 7. Construction of a periodic configuration.** The configuration shown here is simplified compared to that used in the study to help visualization ($R_{tore}$ = 100, $N_{coils}$ = 100). The initial torus is shown in (a) before and in (b) after application of the periodic boundary conditions. Fiber segments appear in green, contacts in red and the nodes are represented by orange spheres.

## V- Discrete memory

To test the presence of discrete memory effects in the entanglements, we applied successive strain paths of varying amplitudes and signs. Discrete and return-point memories were observed in all samples where the fibers deformed elastically, both experimentally and numerically. We show here two examples obtained on the reference periodic configuration and subjected to different strain paths shown in Supplementary Figs. 4(a) and (b).

In Supplementary Figs. 4(a), we performed 2 strain cycles starting either in compression or tension. If we consider the compression first, we start in A and perform an initial compression to B at -2% strain. We then decompress the system to C at -1% strain, and recompress the system down to D at -3% strain, before stretching the system back to zero strain in E. The mirror strain path was also applied in tension through A-B'-C'-D'-E'. Discrete memory is clearly visible here with the B-C and B'-C' loops fully embedded into the main A-D-E and A-D'-E' strain cycles.

In Supplementary Figs. 4(b), we consider another succession of strain cycles going both in tension and compression. We start in A and compress down to B at -1% strain. We then stretch the system to C at +1% strain. The system is then recompressed to -1% strain and comes back precisely to point B, thus showing a return-point memory effect. Another smaller strain cycle, to E at 0 strain and back down to -1% strain brings the system back again to point B. We also performed a tension to B' at +1% followed by compression down to -1% strain, where again the system passes through point B, thus exhibiting return-point and discrete memories.

DOI: 10.1038/NMAT4429

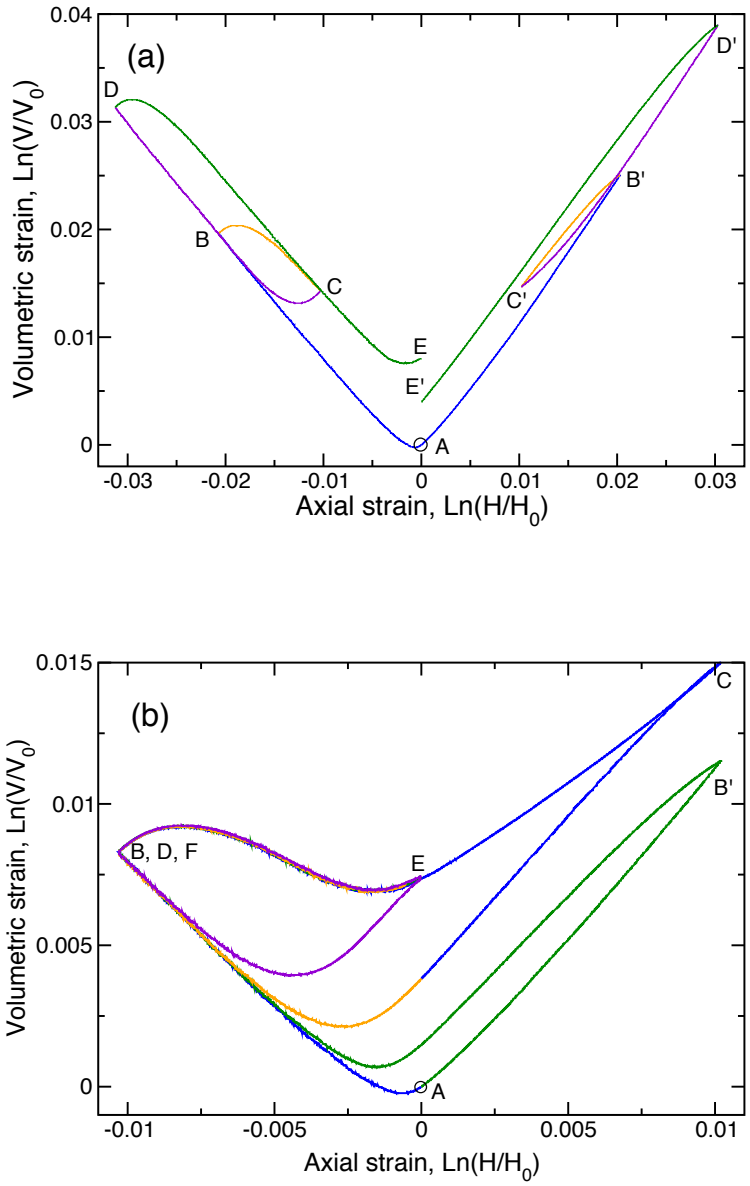


**Supplementary Figure 8. Evolution of volumetric strain during complex strain paths.** The reference periodic configuration was subjected to complex strain-paths following the turning points in alphabetic order. In (a), starting from A, a closed loop is formed between B and C, which is fully enclosed in the larger A-D-E loop. In tension, the discrete memory is less perfect but the sub-loop B'-C' is very close to be closed. In (b), starting from A and going in compression (B) then tension (C) and back in compression (D), the system follows the same path (D-E) as during the initial decompression (B-C). Upon recompression (E-F), we return on the initial compression curve (A-B) exactly at the turning point B=D=F, confirming the discrete memory effect.

## VI- Eight-chain model

To predict the variation of Poisson's function from the knowledge of the average length $\langle \ell \rangle$ and azimuthal angle $\langle \phi \rangle$ of the axis vector, we employ an eight-chain model (Ref. 47 of main text), where the deformation of the entanglement is assumed to arise from the deformation of a model unit cell shown in Fig. 4(c). We assume that the cell has a square basis of length *L*, to reflect the transverse isotropy of the sample and a height *H*. The cell diagonals have length $\langle \ell \rangle$ and azimuthal angle $\langle \phi \rangle$, as shown in Fig. 4c. It is then straightforward to show that geometrically, we have:

$$H = \langle \ell \rangle \cos\left(\langle \phi \rangle\right) \quad \text{and} \quad \mathrm{L} = \langle \ell \rangle \sin\left(\langle \phi \rangle\right) / \sqrt{2} \,. \tag{1}$$

Poisson's function is then given by the negative ratio of the incremental lateral strain ($dL/L$) with respect to the incremental axial strain ($dH/H$):

$$\nu = -\frac{dL / L}{dH / H}. \tag{2}$$

We measure on the simulations the evolutions of $\langle \ell \rangle$ and $\langle \phi \rangle$, from which we compute the evolutions of *H* and *L* using Eq. (1). We then use Eq. (2) to compute numerically the evolution of Poisson's function shown in Fig. 4(d) of the main text.

These variations compare very well with the full simulations, showing that the behavior of Poisson's function is controlled by the rotation and stretching of the axis vectors along the fiber.

DOI: 10.1038/NMAT4429

## VII- Influence of the initial relative density of the samples

We consider here the influence of the initial relative density of the samples. We performed simulations on periodic samples of initial relative density varying between 27% and 42%. We see in Supplementary Fig. 9 that below 33%, the entanglement is not strong enough to allow for a stress to build up in compression and also, to allow for large variations of Poisson's function. At low relative densities, Poisson's function is in fact similar to idealized simulations without contacts (see Fig. 3 of the main text). On the other hand, above 33%, increasing the initial relative density increases Poisson's function in compression and although more weakly, decreases Poisson's function in tension.

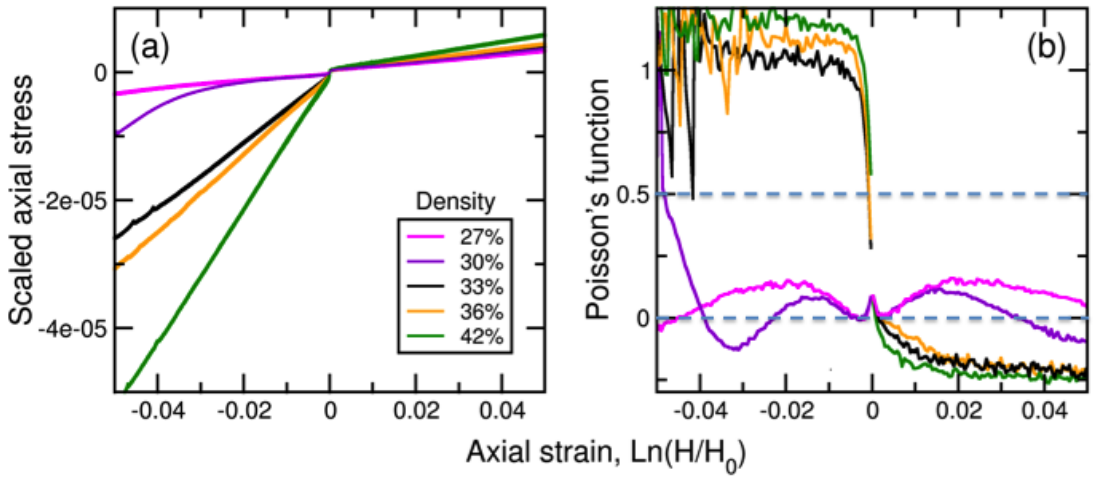


**Supplementary Figure 9. Effect of the relative density on mechanical properties.** Evolution of (a) the scaled axial stress and (b) Poisson's function, during the uniaxial deformation of periodic samples of different relative densities noted on the figure.

We expect that at very large relative densities, the effect on Poisson's function should disappear because the number of initial contacts between fiber segments would be so large that the fiber would not be able to rearrange during deformation and would be forced to follow conventional volumetric strain paths, where Poisson's function remains within the usual bounds. Therefore, we expect the unusual Poisson's functions to appear only in a regime of intermediate relative densities.

Similarly, we have shown in the main text that the effect on Poisson's function disappears if the curvature is very small. Probably, if we considered very strongly curved helices, the effect would also disappear because there would again be too many contacts in the initial configuration to allow for rearrangements. Therefore, if we generalize our study to a parameter plane including the relative density and the equilibrium curvature, we expect to find the effect on Poisson's ratio only in a regime of intermediate relative densities and curvatures. Studying more quantitatively the boundaries of this region is however left for a future paper.

## VIII- Influence of friction

A friction between segments was implemented in the discrete element simulations as tangential springs added between contact points and maintained until the tangential force in the spring was larger than the normal force arising from the repulsive contact potential multiplied by a friction coefficient, μ. More details about the implementation of friction can be found in Ref. 8 of the main text. In tension, adding friction has a negligible effect because contacts play a limited role under tension. On the other hand, in compression, friction limits fiber rearrangements and as a result, decreases Poisson's function as seen in Supplementary Fig. 10. Note however that Poisson's function remains above ½ at least for friction coefficients up to 0.4.

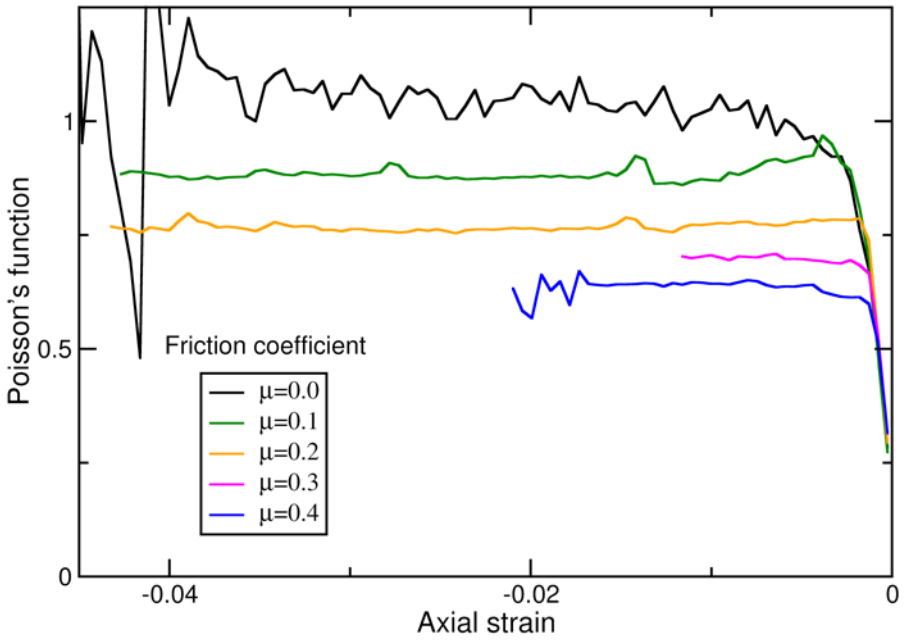


**Supplementary Figure 10. Effect of friction on Poisson's function in compression.** Evolution of Poisson's function during the compression of the reference periodic configuration with varying friction coefficients given in the Figure.

In the experiments, we have not purposely changed the friction coefficient of the wires, for instance by adding a lubricating oil, but we have considered three different materials with different intrinsic friction coefficients. In particular, metals are known to have rather high friction coefficients (above 0.5), while polymers have low friction coefficients (below 0.5), and we have seen in Fig. 1 of the main text that after scaling, polyamide and NiTi wires behave similarly. We therefore expect that friction plays a limited relative role in the present conditions of deformation.

DOI: 10.1038/NMAT4429

## References

[1] G. Wahnström, Phys. Rev. A **44**, 3752 (1991).
[2] P. Koziatek, J.L. Barrat, D. Rodney, Phys. Rev. B **87**, 224105 (2013).
[3] D. Rodney, M. Fivel, R. Dendievel, Phys. Rev. Lett. **95**, 108004 (2005).